Energy Advances

ROYAL SOCIETY OF CHEMISTRY

PAPER

View Article Online
View Journal | View Issue

Cite this: *Energy Adv.*, 2025, 4, 1130

Operando analysis of water transport in zero-gap CO_2 electrolysis cells†

Masakazu Yamagiwa,* Naoya Fujiwara, Yusuke Kofuji and Ryota Kitagawa

The movement of water in zero-gap CO_2 electrolysis cells from the anode side to the cathode side may potentially hamper CO_2 transport to the reduction catalyst, ultimately resulting in reduced CO production. To help prevent this, it is desirable to understand where and how water accumulates. Dynamic water transport in zero-gap CO_2 electrolysis cells was visualized by both visible light and X-ray *operando* imaging. The water breakthrough to the cathode gas channel was visualized by visible light camera observation, while the water seepage through the membrane-electrode assembly was visualized by X-ray radiography. Each frame from the X-ray radiography video was converted to a spatial map of the liquid saturation, and the consecutive frames were used to calculate the liquid flux from the anode to the cathode. This quantitative analysis provides insight into the locations of water accumulation, which tended to occur under the ribs. The flux data showed that, when the water accumulated in the cathode to a certain extent, breakthrough to the cathode flow channel became significant, and water migration from the cathode parts under the ribs to that facing the flow channel also proceeded.

Received 23rd April 2025,
Accepted 10th July 2025

DOI: 10.1039/d5ya00111k

rsc.li/energy-advances

Introduction

The electrochemical reduction of CO_2 to industrial raw materials such as CO and ethylene-glycol can help minimize the CO_2 gas released to the environment.[1–3] Recently, zero-gap type electrolysis cells, where the cathode, membrane and anode are directly attached, have been commonly used for the electrochemical CO_2 reduction. CO_2 electrolysis using zero-gap type electrolysis cells enables high throughput conversion of CO_2 to the desired products.[4] CO_2 electrolysis cells have been shown to operate at high current densities. Specifically, CO_2 electrolysis cells operating at up to 700 mA cm^{-2} have been reported.[2] The high current densities are partially due to the direct supply of CO_2 gas to the cathode catalyst layer *via* a gas diffusion layer (GDL). However, such pathways may be blocked by liquid and/or solid formation in the GDL pores, leading to instability of the cell and eventually to its performance degradation. If the CO_2 gas pathways and/or the gas/catalyst interface become flooded with water, CO_2 gas cannot effectively diffuse to the catalyst surface, and side-reactions such as water reduction (hydrogen evolution reaction, HER) begin to dominate. The HER may also occur if the flow of CO_2 gas to the catalyst surface is impeded by the formation of solid salts, resulting from the reaction of CO_2 gas with the electrolyte cations (such as K^+).[4] Salt formation can be mitigated with the introduction of water vapor into the CO_2 gas flow. However, the introduction of water vapor could also accelerate the local flooding, making it difficult to maintain a proper balance of water inside the cell. Water management is crucial for the extended and stable operation of CO_2 electrolysis cells at the commercial scale.

Water management requires accurate knowledge of the water transport in the cells, which is a dynamic process and is dependent on the operational parameters. X-ray imaging is an effective tool for visualizing inside an operating cell, and the imaging of water movement in polymer electrolyte fuel cells has been reported.[5–8] In the case of CO_2 electrolysis cells, indirect evidence of water flooding and/or salt formation has been reported *ex situ*,[4] and *operando* observations of water transport and catalyst degradation[9–12] have used Cu or Ag cathode catalysts in their experiments. Although Cu has long been a standard material for the fundamental study of CO_2 reduction reactions, CO_2 electrolysis with a Cu catalyst results in various liquid and gas products,[13] making flooding analysis difficult. The present study reports on water transport using Au nanoparticles as cathode catalyst materials. Au catalysts produce mainly CO gas, with H_2 as a side-product, making analysis of water transport relatively straightforward. Water transport in a CO_2 electrolysis cell using an Au nanoparticle catalyst was analyzed by cross-sectional X-ray *operando* imaging of the flow channels and the membrane electrode assembly (MEA) which consisted of a cathode, an anode, and a membrane. The through-plane cathode flow channel observation was conducted simultaneously by using a visible light camera. The X-ray images were processed to obtain

Corporate Laboratory, Toshiba Corporation, Kawasaki, Kanagawa 212-8582, Japan. E-mail: masakazu.yamagiwa@toshiba.co.jp

† Electronic supplementary information (ESI) available. See DOI: https://doi.org/10.1039/d5ya00111k

the spatial and temporal distributions of liquid saturation within the cell. It was found that water tends to accumulate in the cathode, specifically under the ribs of the flow plates. It was also observed that water eventually reached the cathode flow channels at higher current densities. The liquid saturation data were further analyzed to obtain liquid flux and the flow rate.

The quantification of the water movement inside the cell provides new insights into the mechanism of flooding and salt precipitation, leading to effective water management and stable cell operation.

Experimental

An overview of the *operando* observation of the CO_2 electrolysis cell by X-rays and visible light is shown in Fig. 1. X-rays were irradiated from the in-plane direction of the cell to obtain cross-sectional transmission images. At the same time, the cathode channel was observed from the through-plane direction with visible light.

Fig. S1.1 (ESI†) shows a detailed structure of the cell. The cell is equipped with carbon flow plates, which mitigate undesired X-ray absorption losses. The 2 mm-thick carbon flow plates are punctured in the through-plane direction to form channels, and a resin plate with 1 mm protrusions fills the channels halfway to seal the channels. The flow channel is in a serpentine pattern and covers an electrode area of 1 cm^2. This resin window allows through-plane visible light observation of the channels with a CMOS camera (Fig. S1.2, ESI†). Using a visible light CMOS camera served as a complementary method to observe through-plane droplet formation in the cathode flow channels. These visual observations helped validate the assumption—used in the mass balance analysis (Section S2.2, ESI†)—that the droplets remained stationary during measurements. The open structure of the cell allowed X-rays to pass unhindered through the carbon flow plates, allowing the in-plane observation of the channels with an X-ray camera. The cell temperature was maintained at 40 °C using 8 heaters located in and around the resin plates. Although resin is generally a poor thermal conductor, it is reasonable that the temperature of the MEA was close to 40 °C, due to the heaters' proximity to the reaction center.

The CO_2 electrolysis performance of the cell was examined prior to the imaging experiment. The details of the preliminary experiment are provided in Section S3, ESI.† As shown in Fig. S3.2 (ESI†), CO Faraday efficiency of *ca.* 90% was recorded at 200 mA cm^{-2} with a cell voltage of *ca.* 3.0 V. At higher current densities, the product selectivity decreased gradually, and hydrogen evolution became dominant.

Unhumidified CO_2 gas of 99.5% purity was supplied to the cathode channels from a compressed cannister, and the flow was regulated with a mass flow controller (MFC) at approximately 21.3 sccm. 0.1 M $KHCO_3$ aq. was circulated to the anode channels at a rate of 5 mL min^{-1}. DC current was supplied directly to the carbon plates from a regulated power supply. The power supply, along with the CO_2 source and MFC, and the $KHCO_3$ source and pump, were all contained in the X-ray hutch. The power supply was operated remotely *via* USB. The cell voltage, temperature, and inlet–outlet pressures were recorded with a digital logger, and also remotely monitored *via* USB. The visible light camera facing the cathode-side resin window was connected *via* USB to a PC outside the hutch, where the video was monitored and recorded.

The X-ray source was a beamline (BL8S2) specifically designated for imaging purposes, operating at the Aichi Synchrotron Radiation Center (Aichi Prefecture, Japan). The X-ray beam was a collimated, 15 keV monochromatic beam which passes through the cell and was observed using an X-ray camera (Hamamatsu C12849-101U). The camera can observe an area of approximately 1.2 cm by 0.7 cm, which makes it possible to cover all five cathode/anode channels at once. To minimize the risk of camera saturation during cross-sectional imaging, measurements were performed at a frame rate of 10 fps with an exposure time of 100 ms. To ensure complete data acquisition, image frames were temporarily stored in memory during measurement and subsequently transferred to a computer in bulk after the session (*e.g.*, approximately 36 000 frames for a

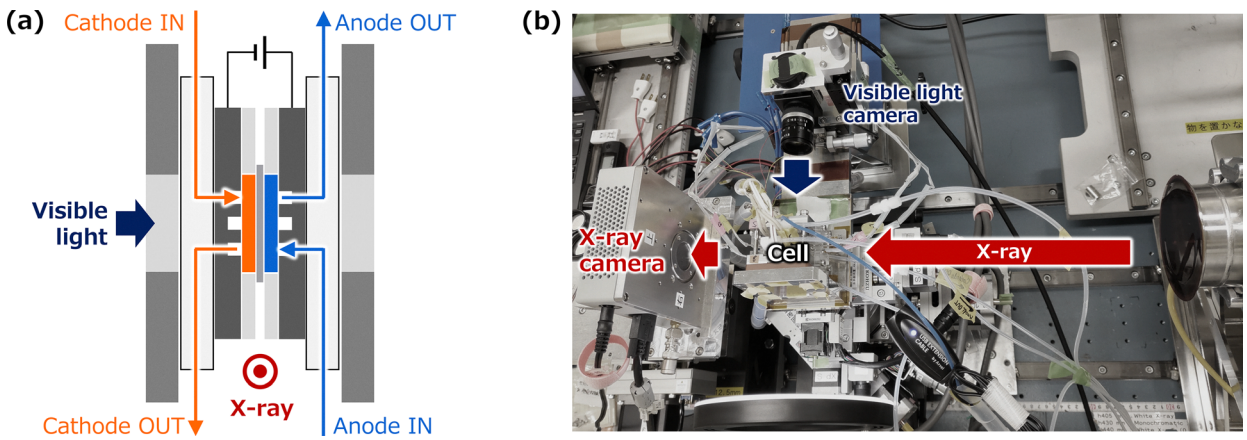

Fig. 1 (a) A schematic diagram of the CO_2 electrolysis cell used in the X-ray *operando* imaging experiments. (b) A photograph of the *operando* setup. The visible light camera was facing the cell perpendicular to the X-ray beam path.

one-hour measurement). A typical measurement was approximately 50 minutes long. This time resolution was chosen to balance temporal details with data transfer rates, allowing us to track water transport dynamics over the time of the experiment.

Results and discussion

The X-ray transmission images reflected the spatial distribution and temporal changes of water saturation in the X-ray analysis cell (Fig. S2.1, ESI†). Before operation, no electrolyte was flowing in the anode flow channel, so there was no X-ray absorption, and both the cathode flow channel and the anode flow channel appeared bright. Immediately after operation started, the anode flow channel appeared dark, and during operation, the anode flow channel appeared slightly bright. This is because the volume of the electrolyte absorbing X-rays decreased due to bubbles generated on the anode side. Also, at the end of operation, the cathode flow channel appeared partially dark because droplets and possibly salts were generated, which absorbed X-rays.

Based on Lambert–Beer's law, it was assumed that the liquid amount in the sample (expressed by liquid depth, the length of water existing along the X-ray beam path) was proportional to the natural logarithm of the intensity ratio of incident light to the sample and transmitted light from the sample. Then, the liquid saturation was calculated using the liquid depth and porosity of the components. The calculation method is detailed in ESI,† Section S2.1. Fig. 2a visualizes the calculation results; spatial distributions of liquid saturation at the start of operation (0 mA cm^{-2}), during operation (400 mA cm^{-2}), and at the end of operation (700 mA cm^{-2}) are shown. Configuration of the cell cross-section is shown in Fig. 2b. The flow direction is explained in Fig. S1.5 (ESI†). The results correspond to the raw X-ray transmission images in Fig. S2.1 (ESI†). As can be seen in Fig. 2a (700 mA cm^{-2}), especially in the bottom most and second-to-bottom cathode flow channel ribs, we could see that water movement progressed, and water accumulated under the ribs. The liquid saturation mapping revealed that liquid saturation in the cathode gas diffusion layer tended to be more pronounced upstream of the CO_2 flow channel. This spatial variation was consistently supported by optical camera observations, which showed more frequent droplet formation in the upstream region.

At the end of operation, liquid saturation value larger than 1 was observed at some locations, for example, under the ribs and near the channel walls. This can be related to the change in the liquid concentration. The liquid depth was calculated based on the X-ray transmittance of 0.1 M $KHCO_3$ aq., but as shown in Fig. S2.3 (ESI†), electrolyte solution of higher concentration absorbs X-rays more strongly. Thus, the liquid depth may have been overestimated if the migrated liquid had condensed. Direct measurement or simulation of the concentration of the migrated liquid is required to take the effect into account, while methods of such measurement and simulation have not yet established and are under development.

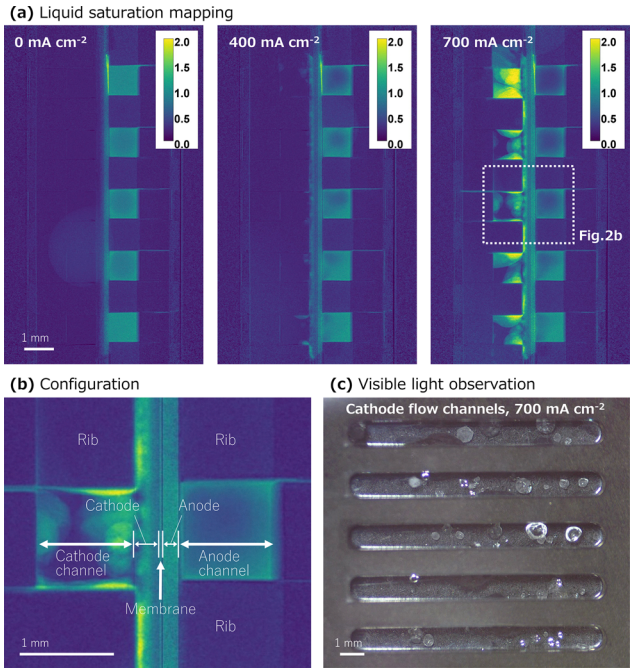

Fig. 2 (a) Liquid saturation maps of a cell cross-section obtained from the X-ray transmission images. The color bar indicates the liquid saturation value. (b) Configuration of the cell cross-section. (c) Visible light photograph of the cathode flow channels at 700 mA cm^{-2}. A video of the liquid saturation mapping over time is provided in the ESI.†

Fig. 2c shows a visible light photograph of the cathode flow channels at the end of the step applying a current density of 700 mA cm^{-2}, corresponding to the far-right mapping result in Fig. 2a. Droplets were generated in the cathode flow channels, penetrating through the MEA. From the through-plane observation, it is possible to determine where droplets were generated in the flow channels, while the in-plane X-ray observation (Fig. 2a) only provides the accumulated information in the depth direction.

The change in cell voltage over time was observed as the applied current density was increased during the operation (Fig. 3a). The cell voltage at each current density was almost identical to that recorded in the preliminary CO_2 electrolysis performance test without X-ray illumination (Fig. S3.2a, ESI†).

This suggests that the electrolysis reaction proceeded successfully. The spikes in cell voltage are likely due to transient effects caused by rapid charge redistribution during the stepwise increase in current density. Compared to the preliminary test (Fig. S3.2a, ESI†), the current in the X-ray imaging experiment was ramped more quickly, which may have amplified these transient responses and resulted in multiple observable spikes.

Beam-induced effects such as potential membrane degradation due to beam exposure were not directly assessed in this study; however, we assumed they were minimal based on prior *operando* wide-angle X-ray scattering studies that reported sustained measurements without observable damage.[9] Furthermore, CO_2 electrolysis experiments conducted with and without X-ray illumination showed similar cell voltages (see Fig. 3(a) and Fig. S3.2(a), ESI†), suggesting negligible impact on membrane behaviour such as H_2 crossover.

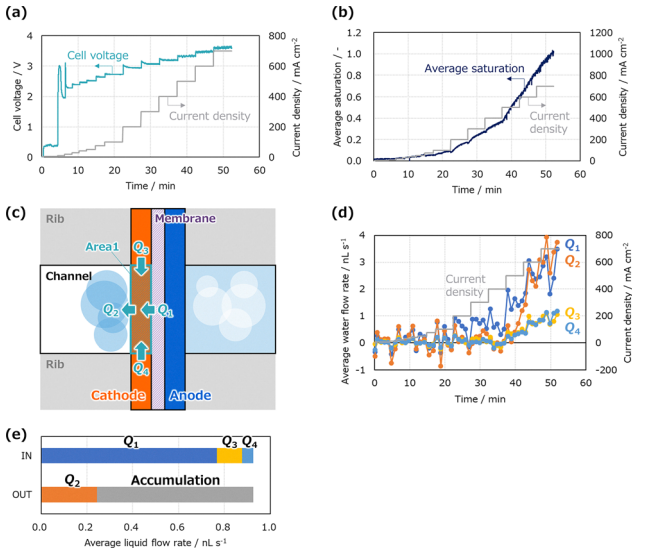

Fig. 3 (a) Current density and cell voltage recorded during the X-ray imaging experiment. (b) Average liquid saturation in Area 1 during the imaging experiment. (c) Schematic image of a cell cross-section illustrating Area 1 and liquid flow rates Q1–Q4. (d) Temporal change of Q1–Q4 in the imaging experiment. (e) Average Q1–Q4 values over 5 minutes with a current density of 300 mA cm^{-2}.

We focused on a cathode portion, consisting of the cathode catalyst layer and GDL (including microporous layer), that contacts the central cathode flow channel (the third of five). The portion is labelled as Area 1 (Fig. 3c). Fig. 3b shows the liquid saturation in Area 1 during the imaging experiment. Because Area 1 is composed of multiple layers, the saturation value was spatially averaged. The saturation increased over time, and the faster the rate of increase in saturation the higher the current density. This may be due to the increase in the ion concentration gradient between the cathode catalyst surface and the bulk liquid phase, and the increase in capillary pressure inside the cathode catalyst layer. The increase in capillary pressure can be brought by the high ion concentration and electrowetting.[14,15] In the low current density range, the saturation sharply increased immediately after the current density was changed, and then tended to settle down. This can be related to the movement of K^+ ions in the following manner: when the current increases stepwise, the concentration of anions (OH^-, HCO_3^-, and CO_3^{2-}) at the cathode also increases rapidly. To maintain charge neutrality, cations, in this case K^+, move towards the cathode from the bulk liquid phase. This movement also attracts water molecules to the cathode reaction field. The effect of K^+ ions accompanying water is significant immediately after a change in current density but stabilizes once charge neutrality is achieved.

Water transport inside the cell was quantitatively estimated by focusing on the temporal change of the liquid amount. Fig. 3c illustrates the cell cross-section including Area 1. By considering the mass balance of Area 1, liquid flux entering and exiting from Area 1 was calculated. The calculation method is detailed in ESI,† Section S2.2. The liquid flow rates from the membrane to Area 1 and that from Area 1 to the adjacent flow channel are denoted as Q1 and Q2, respectively. The liquid flow rates from cathode parts contacting ribs are denoted Q3 and Q4. The flow rates were obtained by multiplying the fluxes by the corresponding areas. Fig. 3d shows the temporal change of Q1 to Q4. All flow rates increased monotonically with the passage of time and the increase in current density. Q1 started to increase at around 200 mA cm^{-2}. The Q1 value tended to stabilize in each current step. Q2, Q3, and Q4 were almost zero until 400 mA cm^{-2}, but rapidly increased after the current density of 500 mA cm^{-2}. When the saturation of the cathode progressed to a certain extent, liquid breakthrough to the adjacent flow channel occurred, resulting in the increase in Q2. In response to this, inflow from the cathode parts under the ribs to Area 1 also occurred. The separation of the contributions of time and current density is not achieved at present but will be possible by analyzing the flow rates with different current profiles where current density values and holding times of each step are systematically varied.

Fig. 3e shows the average Q1 to Q4 values over 5 minutes when a current density of 300 mA cm^{-2} was applied. This graph visualizes the liquid mass balance in Area 1. The upper bar shows the inlet liquid flow rates (Q1, Q3, and Q4). The outlet flow rate Q2 is shown in the lower bar, and the balance corresponds to the liquid accumulation in Area 1. This liquid accumulation is the cause of the increase in saturation (Fig. 3b). As the result at 300 mA cm^{-2} is shown in Fig. 3e for example, the same analysis can be applied for all current densities. At lower current densities, formation of droplets in the cathode flow channel was not significant, and most of the inlet liquid was accumulated in Area 1. At higher current densities, the portion of liquid accumulation decreased because droplet growth proceeded, although the absolute amount of the accumulated liquid increased with the current density.

The cathode outlet gas composition was not measured by gas chromatography in the present X-ray imaging experiment, but it is reasonable to assume that the selectivity for CO decreased while the H_2 evolution became dominant with increasing current density, referring to the cathode Faraday efficiency result of the preliminary experiment (Fig. S3.2b, ESI†). The CO_2 flow rate at the cathode inlet was 21.3 sccm and 20 sccm in the X-ray imaging experiment and the preliminary experiment, respectively. These rates correspond to >200% of the theoretically required CO_2 flow rate at 700 mA cm^{-2}. This means that H_2 evolution proceeded at high current densities despite the sufficiently high CO_2 concentration in the cathode flow channel. The migrated liquid in the cathode catalyst layer, GDL, and flow channel may have hindered the CO_2 diffusion to the cathode catalyst surface, leading to the insufficient CO_2 supply at the cathode catalyst surface and the low CO selectivity. To account for the possibility of CO_2 crossover to the anode side *via* anion transport—particularly CO_3^{2-}, which can carry twice the molar amount of CO_2—we calculated the CO_2 conversion ratio at each current density using a mass balance approach that includes crossover effects. These results are provided in tabular form in the Table S3.1, ESI.†

The present method offers a quantitative understanding of the water transport in zero-gap CO_2 electrolysis cells. Analysis

of liquid flux and flow rates under various operating conditions and cell material conditions will contribute to clarify the mechanism of flooding. The quantitative evaluation of the water transport is also important for establishing numerical models which simulate the water transport and its effect on the cell performance.[4,16] Such models can be used to control electrolysis systems and to predict the lifetime of cell stacks.

Conclusions

Operando X-ray imaging of a zero-gap CO_2 electrolysis cell was performed to investigate the water transport inside the cell. Based on the X-ray transmission images, the liquid amount and saturation were calculated and visualized. The result was further analyzed to quantify the liquid flux and flow rate. The influx, efflux, and accumulation of the liquid at the cathode portion adjacent to the central flow channel were determined by considering the mass balance. It was found that the liquid flow rates varied depending on the elapsed time and applied current density. Acquiring water transport data under various conditions using the present method will contribute to clarify the mechanism of cathode flooding and salt precipitation, and to develop numerical simulation models.

Author contributions

MY: investigation, methodology, conceptualization, formal analysis, visualization, writing – original draft, and writing – review and editing; NF: investigation, methodology, conceptualization, formal analysis, visualization, writing – original draft, and writing – review and editing; and YK: writing – review and editing; and RK: supervision.

Conflicts of interest

There are no conflicts to declare.

Data availability

Any data that support the finding of this study are included within the article and also included as a part of the ESI.†

Acknowledgements

The authors would like to express their sincere gratitude to M. Yoshiki and M. Oki for their invaluable expertise and guidance with the X-ray *operando* imaging experiments, as well as for their many insightful discussions. The authors would also like to thank H. Hirazawa and H. Sumi for their valuable contributions to the design, construction, and wiring of the CO_2 electrolysis cell.

References

1 J. Tamura, A. Ono, Y. Sugano, C. Huang, H. Nishizawa and S. Mikoshiba, *Phys. Chem. Chem. Phys.*, 2015, **17**, 26072–26078.
2 Y. Kofuji, A. Ono, Y. Sugano, A. Motoshige, Y. Kudo, M. Yamagiwa, J. Tamura, S. Mikoshiba and R. Kitagawa, *Chem. Lett.*, 2021, **50**, 482–484.
3 Y. Kudo, A. Ono, S. Mikoshiba and R. Kitagawa, *Sustainable Energy Fuels*, 2024, **8**, 2649–2658.
4 M. Sassenburg, M. Kelly, S. Subramanian, W. A. Smith and T. Burdyny, *ACS Energy Lett.*, 2023, **8**, 321–331.
5 R. Guan and A. Bazylak, *Electrochim. Acta*, 2023, **447**, 142103.
6 W. Yoshimune, A. Kato, S. Yamaguchi, S. Hibi and S. Kato, *ACS Appl. Mater. Interfaces*, 2024, **16**, 36489–36497.
7 W. Yoshimune, Y. Higuchi, A. Kato, S. Hibi, S. Yamaguchi, Y. Matsumoto, H. Hayashida, H. Nozaki, T. Shinohara and S. Kato, *ACS Energy Lett.*, 2023, **8**, 3485–3487.
8 A. Kato, S. Kato, S. Yamaguchi, T. Suzuki and Y. Nagai, *Int. J. Hydrogen Energy*, 2024, **50**, 1218–1227.
9 A. B. Moss, S. Garg, M. Mirolo, C. A. G. Rodrigues, R. Ilvonen, I. Chorkendorff, J. Drnec and B. Seger, *Joule*, 2023, **7**, 350–365.
10 J. Disch, L. Bohn, S. Koch, M. Schulz, Y. Han, A. Tengattini, L. Helfen, M. Breitwieser and S. Vierrath, *Nat. Commun.*, 2022, **13**, 6099–6107.
11 A. B. Moss, J. Hätinen, P. Kúš, S. Garg, M. Mirolo, I. Chorkendorff, B. Seger and J. Drnec, *J. Power Sources*, 2023, **562**, 232754.
12 Q. Xu, J. Z. Zeledón, B. O. Joensen, L. Trotochaud, A. Sartori, L. Kaas, A. Moss, M. Mirolo, L. Mairena, S. Huynh, S. Garg, S. Helveg, I. Chorkendorff, S. Zhao, B. Seger and J. Drnec, *Nat. Nanotechnol.*, 2025, **20**, 889–896.
13 Y. Hori, R. Takahashi, Y. Yoshinami and A. Murata, *J. Phys. Chem. B*, 1997, **101**, 7075–7081.
14 M. Li, M. N. Idros, Y. Wu, T. Burdyny, S. Garg, X. S. Zhao, G. Wang and T. E. Rufford, *J. Mater. Chem. A*, 2021, **9**, 19369–19409.
15 F. Mugele and J.-C. Baret, *J. Phys.: Condens. Matter*, 2005, **17**, R705–R774.
16 B. A. McCain, A. Stefanopoulou and I. V. Kolmanovsky, *Chem. Eng. Sci.*, 2008, **63**, 4418–4432.